Additive Manufacturing 46 (2021) 102179

Contents lists available at ScienceDirect

Additive Manufacturing

journal homepage: www.elsevier.com/locate/addma

Research Paper

An investigation of the plastic work to heat conversion of wrought and laser powder bed fusion manufactured Inconel 718

John Varga [a], Owen T. Kingstedt [a,*]

[a] Department of Mechanical Engineering, University of UTah, Salt Lake City, UT 84112, USA

ARTICLE INFO

Keywords:
Split-Hopkinson pressure bar
Thermo-mechanics
Additive manufacturing
Inconel 718
Taylor-Quinney coefficient
Dynamic behavior of materials

ABSTRACT

In this study, the conversion of plastic work to heat, also known as the Taylor-Quinney coefficient (β), of Inconel 718 (IN718) is investigated. Three material conditions are examined, specifically wrought IN718 and laser powder bed fusion (LPBF manufactured IN718 in the as-built condition and one that has been recrystallized through a solutionizing heat treatment. Adiabatic deformation conditions are achieved using a tension split-Hopkinson pressure bar. Infra-red thermography measurements are made during deformation such that the conversion of plastic work to heat can be determined for each material condition as a function of strain. Microstructure characterization was conducted using electron backscatter diffraction to measure grain size, morphology, and texture. From the experiments conducted, it was observed that wrought IN718 had the lowest conversion of plastic work to heat ($\beta \approx 0.2$). The as-built LPBF IN718 had a slightly higher conversion of plastic work to heat ($\beta \approx 0.3$), and the recrystallized condition had the greatest plastic work to heat conversion ($\beta \approx 0.45$). The observed ordering of the plastic work to heat conversion efficiency is discussed in light of the microstructural similarities and differences of each material condition. Increasing grain size was found to be correlated with a decrease in β.

1. Introduction

Inconel 718 (IN718) is a precipitation-hardened nickel-based super alloy. Its excellent corrosion resistance and high strength at elevated temperatures ($> 700^{\circ}$C) make it a commonly used structural material for extreme environments such as those seen in aerospace applications. The high-strength properties of IN718 are due to the distribution of the precipitated Ni_3Nb body centered tetragonal γ'' phase and the $Ni_3(Al,Ti)$ face centered cubic (fcc) γ' phase [1–3]. Of these two phases, the γ'' phase is the primary strengthening precipitate because it produces a coherency strain with the matrix up to 2.9%, while the γ' phase produces a coherency strain of less than 1.25% [4]. In traditionally manufactured IN718, coprecipitate γ'/γ'' structures have been observed. Coprecipitate structures have been demonstrated to require complex dislocation structures to induce plastic deformation, resulting in improved mechanical properties [5,6]. To the authors' knowledge, the coprecipitate structure has yet to be observed in additively manufactured (AM) IN718.

Prolonged heat treatments (> 100 h) can transform the meta-stable γ'' phase to the stable Ni_3Nb orthorhombic δ phase, which has been shown to restrict grain growth and diminish grain boundary creep fracture [7,8]. The generally undesirable Laves phase, consisting of $(Ni,Fe,Cr)_2(Nb,Mo,Ti)$, occurs due to the poor diffusibility of Nb and is often observed in the segregation region of laser-powder bed fusion (LPBF) IN718. The brittle nature of the Laves phase leads to mechanical property reductions. Therefore, solutionizing heat treatments are often employed to dissolve the Laves phase to release key elements (e.g., Ti) back into the matrix to increase strengthening γ' and γ'' phase precipitation.

IN718 has become a popular alloy in additive manufacturing research community with review articles (e.g., [9]) and books (e.g., [10]) covering it's mechanical properties. Additive manufacturing has significant promise to enable the fabrication of complex geometry components, such as engine turbine blades with integrated cooling channels. However, the as-printed surface quality of AM components is typically lower than traditionally machined components. Surface asperities lead to stress concentrations which in turn result in lower-than-desired mechanical performance. One approach to improve the mechanical properties of AM components is to incorporate traditional subtractive machining methods during the AM process to improve surface finish [11,12]. In this hybrid approach, the AM build process and

---

* Corresponding author.
E-mail address: o.kingstedt@utah.edu (O.T. Kingstedt).

https://doi.org/10.1016/j.addma.2021.102179
Received 2 April 2021; Received in revised form 15 June 2021; Accepted 8 July 2021

machining step alternate, leading to increased build times. To reduce machining times, a thorough understanding of a material's thermo-mechanical behavior is necessary, particularly for alloys such as IN718 that present challenges in machining [13,14]. One of the motivations of the current work is to report the conversion of plastic work to heat under adiabatic conditions for IN718, which is needed to enable accurate modeling of high-speed machining processes that could be incorporated into hybrid AM approaches to alleviate bottlenecks during component production.

In addition to surface roughness, internal porosity can have an impact on component mechanical properties. There has been a large body of work dedicated to the study of porosity in LPBF metals (e.g., [15–18,19]). Porosity within components is categorized into three main categories: gas pores, keyhole pores, and lack of fusion pores [20]. Gas pores tend to be smaller and spherical in nature, where keyhole and lack of fusion pores are comparatively larger and are non-spherical. Keyhole pores form when an energy density greater than the optimal density is used [21,22]. Lack of fusion pores are common when an insufficient energy density is used. A recent assessment of pore type within an LPBF IN718 build conducted by Watring et al. [23] found spherical gas pores to account for less than 0.3% of the entire build volume across three separate build volumes that were produced using different combinations of laser power and build orientation. Under quasi-static tension conditions, it was found that for the same laser energy density similar tension yield strength behavior was observed despite differences in porosity and build orientation. Babamiri et al. [24] recently investigated the porosity distribution of LPBF IN718 subjected to a stress relieving heat treatment and hot isostatic pressing. They found that porosity was greatest near the print surface periphery, and minimal at the printed component interior. Kumar et al. [25] performed a systematic study of laser power and scan speed to achieve high density (≥99%) LPBF components. Proper selection of process parameters resulted in fully-dense porosity free LPBF IN718. Therefore, careful extraction of specimens from the interior of a build volume produced using optimized process parameters, such as those recommended by manufacturers, results in specimens that can be approximated as fully-dense and porosity free.

During plastic deformation, a portion of plastic work, commonly referred to as cold work, is stored within a material through defects (e.g., dislocations, deformation twins, residual strains), while the remainder is converted into heat [26–29,30,31]. The efficiency of the conversion of plastic work to heat is commonly known as the Taylor-Quinney coefficient or β coefficient [27]. This coefficient is the macroscopic manifestation of lower length scale processes including but not limited to dislocation generation, dislocation glide, dislocation entanglement, dislocation annihilation and deformation twinning. An understanding of the Taylor-Quinney coefficient is of critical importance for developing accurate temperature-dependent constitutive models and predicting the onset of thermoplastic instabilities during deformation [29–32,33]. Specific applications requiring an understanding of the Taylor-Quinney coefficient include, high-speed machining, ballistic performance, shear band formation, and dynamic fracture.

Quasi-static deformation strain-rates present an iso-thermal loading condition where heat that is generated locally can dissipate at a rate faster than the rate of deformation. Conversely, dynamic strain-rates (e.g., $\varepsilon > 10^2 s^{-1}$) can essentially be treated as adiabatic processes, where specimen temperature rises can be significant [29–31,34]. Traditionally, the Taylor-Quinney coefficient has been approximated to be a constant value of ninety percent ($\beta = 0.9$), and can be represented in terms of the integral-based ratio of thermal dissipation to mechanical work (β_{int}) or the differential-based rate of dissipation of mechanical power (β_{diff}). An important distinction between β_{int} and β_{diff} is that $\beta_{int} \leq 1$, unless an additional latent heat source, such as a phase transformation, occurs during deformation. The stored energy of cold work quantity is then, $f = 1 - \beta_{int}$. Regardless of Taylor-Quinney coefficient reported (β_{int} vs. β_{diff}), simultaneous measurement of the specimen temperature rise, stress, and strain are required. The approximation of $\beta = 0.9$, and thus stored energy $f = 0.1$, has been shown to be an over simplification, as experimental efforts have demonstrated these quantities to vary with strain [30,35], strain-rate [29,35,36], loading mode [34], grain size [37–39], crystallographic loading orientation [40], and active deformation mechanisms [41]. A tabular overview of the variation of the Taylor-Quinney coefficient from experiments conducted on a range of materials can be found Ref. [34].

Modeling efforts have attempted to rationalize the range in reported Taylor-Quinney coefficient values and stored energy data obtained from experiments. A few models are discussed in the following to showcase the range of approaches and variations in model complexity that have been reported. Zehnder [42] presented a straightforward model correlating strain hardening to dislocation density and once a limited set of variables were tuned, was able to model experimental data of polycrystalline Cu. Aravas et al. [43] proposed a simple model based on calculating the energy associated with residual stresses after plastic deformation and unloading. Their model showed that at large strains a material's hardening exponent provides the upper bound for the ratio of stored energy to energy dissipated as heat. Kapoor and Nemat-Nasser [44] used an energy change caused by dislocation density evolution approach, and found that only a small amount (1%) of plastic work is stored as dislocations within the material. Rosakis et al. [45] presented a classical thermoplasticity model based on an internal variable model restricted by the second law of thermodynamics, and simplified by experimentally-motivated assumptions. Their thermoplasticity model was demonstrated to capture experimentally observed strain and strain-rate dependence of β in rate-sensitive α-Titanium, and rate-insensitive Al 2024. The work of Benzerga et al. [46] adopted a dislocation dynamics approach to directly model individual dislocations during plastic deformation and the corresponding evolution of the Taylor-Quinney coefficient. They found the Taylor-Quinney coefficient to be dislocation density and dislocation mobility dependent. The recent molecular dynamics study of Kositski and Mordehai [47] investigated dislocation motion in single crystals and grain boundary evolution in nanograined materials. They found that dislocation glide, and grain boundary processes of dislocation nucleation and dislocation annihilation result in a nearly complete conversion of work to heat (i.e., $\beta = 1$). Additionally, they observed that an increase in the grain boundary volume fraction results in greater internal energy storage (i.e., lower Taylor-Quinney coefficient), and a decrease in the grain boundary volume fraction releases internal energy (i.e., higher Taylor-Quinney coefficient). Lieou and Bronkhorst [48] recently developed a partitioned-energy thermodynamic framework to quantify the differential Taylor-Quinney coefficient. Their framework suggests that the Taylor-Quinney coefficient is material dependent and increases with increasing strain.

To date, thermo-mechanics studies reporting experimentally measured Taylor-Quinney coefficients have largely been conducted under high-strain-rate compression or shear-dominated loading. Comparatively, the assessment of the thermo-mechanical conversion of work to heat for materials under high-strain rate tensile deformation is relatively scarce. Notable examples include, Macdougall and Harding [49], Xia and Rao [50], and the work of Rittel et al. [34]. With the Taylor-Quinney coefficient being loading mode dependent, one objective of this study is to fill a knowledge gap in our understanding of the tensile thermo-mechanical coupling of IN718. Furthermore, thermo-mechanics studies have tended to focus on a single material preparation condition. It is well established that AM metals have drastically different microstructures than their wrought counterparts. Thus, the second objective of the presented work is to investigate the variation in the conversion of plastic work to heat as a function of material preparation, specifically comparing IN718 of the wrought condition to its AM counterparts. IN718 was judiciously selected for this study because the as-built LPBF microstructure has a dense dislocation cell network and limited presence of primary γ' and γ'' strengthening phases [51]. These two features are in stark contrast with the wrought condition which has a low initial dislocation density and has an optimized distribution of primary strengthening phases throughout its microstructure. A recrystallized condition obtained from solutionizing the as-built condition is also examined. Collectively, the three dramatically different microstructures provide the opportunity to obtain understanding of the specific microstructure features in IN718, including γ' and γ'' strengthening presence, initial dislocation density, secondary δ phase presence, and grain size, that impact energy storage and the conversion of plastic work to heat efficiency under adiabatic deformation.

Lastly, there have been limited investigations targeted at assessing the dynamic behavior of LPBF IN718. To the authors' knowledge, there has only been one previous study by Babamiri et al. [24] to investigate the dynamic tension behavior of LPBF IN718, and no studies have been reported investigating the thermo-mechanical behavior of any AM metal.

2. Methodology

2.1. Specimen fabrication

Source material for the wrought IN718 condition was purchased in a 3.175 mm thick annealed sheet meeting ASTM B670 [52] and AMS5596 [53]. Specimens were extracted from the sheet using waterjet cutting to the dimensions provided in Fig. 1. The loading direction of the waterjet cut specimens was selected to be parallel to the sheet rolling direction.

The as-built condition was produced using LPBF on a Concept Laser using $+45$–10 μm virgin powder and manufacturer recommended process parameters (i.e., 53 μm spot size, 160 W laser power, 680 mm/s scan speed, 5 mm by 5 mm islands on a checkerboard pattern). Two blocks with in-plane dimensions of 80 mm by 80 mm with a 100 mm build height were produced. The first block was removed from the build plate and no post-build heat treatments were applied. The decision to forego post-build heat treatments was motivated by the desire to maintain internal residual stresses and the dense dislocation cell network that occurs as a result of the rapid solidification rates intrinsic to the LPBF process. The second block was removed from the build plate and subjected to a solutionizing heat treatment. The solutionizing treatment consisted of a 10.5 ˚C/min ramp-up rate, one-hour dwell at 1250 ˚C, and 10.5 ˚C/min ramp-down rate. The motivation for applying the solutionizing heat treatment was to completely eliminate the LPBF process residual stresses, dislocation cell network, and solidification direction dictated texture from the material. The solutionizing heat treatment exceeds the 1100 ˚C recrystallization temperature of IN718. Therefore, an equiaxed microstructure is obtained upon completion of the heat treatment. From each block, specimens with dimensions identical to the wrought condition were extracted using wire electrical discharge machining (EDM). As-built and recrystallized specimens were extracted so their loading axis is parallel to the build direction of the LPBF process, see Fig. 1.

The use of manufacturer recommended build parameters and the removal of specimens from the internal region of the build volume limits the level of porosity that would be present throughout their gauge section to the point that the as-built and recrystallized specimens are considered by the authors to be fully dense and porosity free. This claim is supported by previous x-ray computed tomography studies conducted by Babamiri et al.[24] and Moorthy [54] which have shown porosity in LPBF IN718 build volumes to be limited to the build volume periphery. Electron microscopy investigations presented in the following section, did not find regions of noticeable porosity due to lack of fusion or keyholing. It is assumed that small scale porosity due to gas inclusion could be present in the as-built case, however as was shown by Watring et al. [23], this small-scale and small-volume porosity does not govern tensile mechanical behavior to a noticeable degree. Instead, as Babamiri et al. [24] and Kantzos et al. [55] have reported, tensile mechanical properties (i.e., yield strength, ultimate tensile stress, % elongation) of LPBF IN718 are governed predominantly by microstructure features.

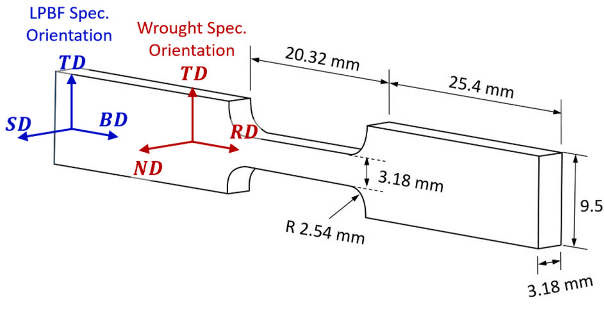

Fig. 1. Tension split-Hopkinson bar specimen dimensions and orientation with respect to principal processing directions for the wrought condition and LBPF condition.

2.2. Microstructure characterization

Specimen surfaces were prepared for microstructural characterization using mechanical polishing. Polishing was performed using progressively finer water-lubricated silicon carbide papers, followed by glycol-based diamond suspensions with the final preparation step using a 0.05 μm silica suspension. Between each of the polishing steps, specimens were cleaned using a Branson 2800 ultrasonic cleaner to limit cross-contamination of polishing cloths.

Once prepared, scanning electron microscope (SEM) micrographs of the specimen surfaces were captured using a Helios Nanolab 650i. Both secondary electron imaging and backscattered electron (BSE) modes were utilized to capture and observe the morphology and distribution of precipitated phases. Electron backscattered diffraction (EBSD) data were captured on a 500 nm hexagonal grid using a 20 kV accelerating voltage, 1.6 nA current, and a working distance of 11 mm. Grain orientation maps were cleaned in OIM Analysis software using neighbor CI correlation of minimum CI 0.3. For each material condition, at least three specimens were examined and the following data was generated for each: measures of average grain size using the line intercept technique, inverse pole figure (IPF) using grain orientation coloring, and a pole figure triad. The EBSD reference direction of the wrought specimens coincides with the specimen's normal direction. For the LBPF specimens in the as-built and recrystallized condition, the reference direction is the sweep direction.

2.3. Adiabatic deformation experimentation

A desirable condition for the study of the conversion of plastic work to heat is an adiabatic deformation process. The time span over which deformation is adiabatic can be estimated by the Fourier number, $F_0 = \alpha t/l^2$, where, α is the material's thermal diffusivity ($\alpha \approx 10^{-5}\ m^2/s$ for metals [56]), t is the loading duration, and l is a characteristic specimen dimension (typically length). When $F_0 < 0.01$, the deformation process is adiabatic. Loading pulse durations (t) and specimen lengths (l) are governed by the experimental technique used. One commonly used experimental technique in high-strain-rate mechanics capable for providing short loading pulse duration ($t < 0.1s$) and short sample length ($l < 0.01$ m), resulting in a Fourier number indicative of adiabatic conditions is the tension split-Hopkinson pressure bar (TSHPB).

The TSHPB setup utilized in this work consists of a 457.2 mm long tubular striker, and 3.658 m long incident and transmitted bars, all made from maraging-steel. At the mid-point of the incident and transmitted bars, two strain gauges are mounted diametrically opposite of each other, wired in a quarter-Wheatstone bridge configuration. The signals recorded for each bar are averaged to eliminate bar bending strains from the reported stress-strain behavior of the material. A typical raw data trace recorded by the strain gauges of the TSHPB is shown in Fig. 2. The representative data shows a pulse duration of

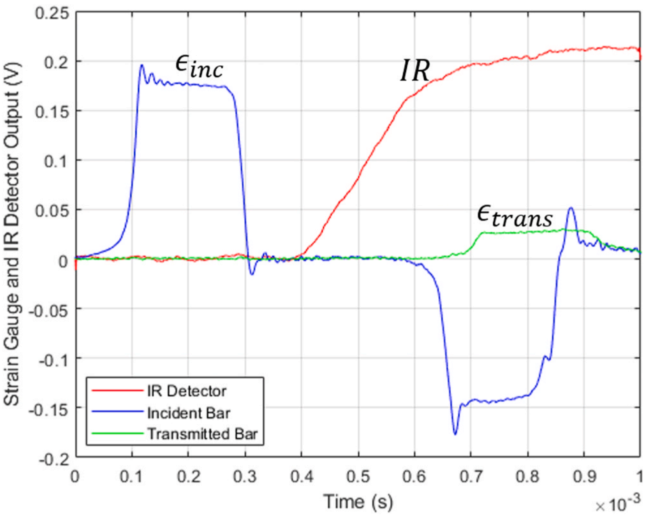

Fig. 2. Representative raw data captured using the TSHPB and IR detector.

$t = 0.25 \times 10^{-3}$ s. For the specimen gauge length of $l = 0.02$ m, the Fourier number of this representative experiment is $F_0 < 0.01$, and therefore can be approximated as adiabatic.

As will be shown in Section 3.2, a single loading pulse may not have been sufficient to cause specimen failure. Thus, multiple loading iterations were used as necessary to fail specimens (i.e, separate into two pieces). Specimen dimensions were measured after each loading increment. Measured dimensions were then used when calculating the material stress-strain behavior for the next loading increment. Additionally, measured dimensions were compared to those predicted by assuming volume conservation to confirm specimen slipping in the gripping region did not occur. Specimen slipping in the grip region was not observed for any of the stress-strain curves reported.

A summary of the one-dimensional wave analysis used to convert strain gauge measurements to the specimen's nominal engineering stress, strain and strain-rate response is presented in the subsequent. For a more in depth presentation on the operation and theory of the TSHPB the reader is encouraged to review Refs. [57,58]. The specimen's nominal strain-rate ($\dot{\epsilon(t)}$), engineering strain ($\epsilon(t)_{spec}$), engineering stress ($\sigma(t)^E_{spec}$), true stress($\sigma(t)^T_{spec}$) and true strain ($\varepsilon(t)_{spec}$) can be calculated assuming one-dimensional wave propagation and the existence of a force balance. The strain-rate of the specimen is calculated as follows:

$$\dot{\epsilon(t)}_{spec} = -\frac{c_0}{L_s}\epsilon_{ref} \tag{1}$$

where, c_0 is the wave speed of the incident and transmitted bars, L_s is the specimen gauge length, and ϵ_{ref} is reflected wave strain in the incident bar. All experiments (i.e., loading increments) were conducted using the same gas-gun pressure to launch the striker tube. This resulted in an average strain rate of 460 s^{-1} with a range of $\pm$ 60 s^{-1} across all experiments reported. This variation in strain-rate does not result in loading-rate dictated variations in material behavior or impact the conversion of plastic work to heat for each loading increment. Integrating the specimen strain-rate over the length of time over which the loading pulse occurs, t, yields the specimen's strain as:

$$\epsilon(t)_{spec} = -\frac{c_0}{L_s}\int_0^t \epsilon_{ref} d\tau. \tag{2}$$

Finally, specimen stress for the square cross-section specimen geometry used in the current work can be solved for by using the following:

$$\sigma(t)^E_{spec} = \frac{E_{bar}A_{bar}\epsilon_{trans}}{t^2_{spec}} \tag{3}$$

where, E_{bar} and A_{bar} are the elastic modulus and cross sectional area of the incident and transmitted bars, respectively, ϵ_{trans} is the transmitted pulse strain, and t_{spec} is the specimen gauge thickness. Once the engineering stress and strain are determined, they are converted to true strain and stress values as follows:

$$\varepsilon(t)_{spec} = -ln(1-\epsilon(t)_{spec}) \tag{4}$$

$$\sigma(t)^T_{spec} = \sigma(t)^E_{spec}(1-\epsilon(t)_{spec}). \tag{5}$$

2.4. Infra-red thermography

During the TSHPB experiments, a liquid nitrogen cooled HgCdTe (MCT) infra-red (IR) detector with a spectral sensitivity of $2\mu m$-$13\mu m$ and Newtonian optical system were used to record the real-time temperature rise of the deforming specimen. Prior to each experiment (i.e., loading increment), the IR detector is calibrated using the approach of J. Hodowany [59] to determine the conversion factor between recorded voltage and specimen temperature. The calibration consists of placing a specimen in the TSHPB and mounting a resistance temperature detector (RTD) to the specimen surface opposite that viewed by the IR detector. An IR spot heater heats the specimen while its temperature is monitored by the RTD. A chopping wheel placed between the specimen and the IR detector, provides a dynamic signal for the IR detector. Once a desired specimen temperature is reached, the IR spot heater is shut-off, the IR detector element is uncovered and the specimen cooling is recorded. The temperature-time output of the RTD and the voltage-time output of the IR detector are then reduced to determine the calibration curve relating IR detector output voltage to specimen temperature (see Fig. 3. The specimen temperature during the TSHPB experiment is determined by converting the measured IR detector voltage to temperature using the calibration curve obtained prior to the deformation increment. Using this approach, the IR detector is calibrated to individual specimens, which ensures that variations in surface finish, caused by variations in specimen preparation or plastic deformation accumulation, are accounted for during the calibration step. A representative calibration curve is shown in Fig. 3, showing a linear relationship between the IR detector output voltage and specimen temperature for temperature rises above 1 °C.

The short time-duration of a TSHPB loading results in adiabatic conditions, where heat conduction is minimized. Thermo-elastic effects are known to be small (0.2 °C) compared to the temperature rise associated with plastic deformation ($>$ 10 °C). Due to their small amplitude, thermo-elastic effects are neglected when determining the plastic work

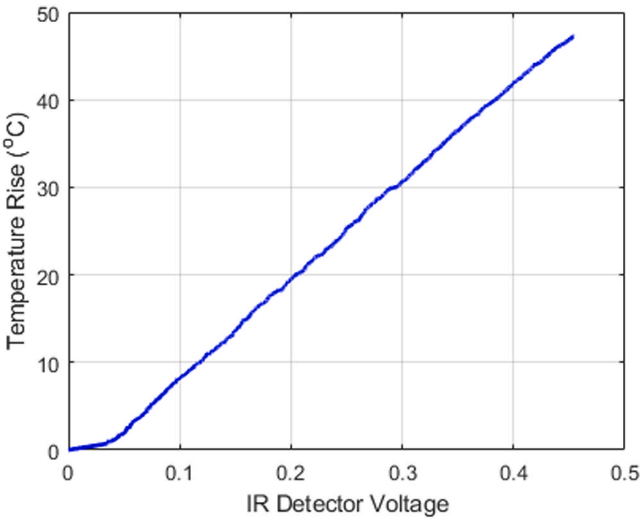

Fig. 3. A representative IR detector calibration curve relating the IR detector output voltage and the specimen temperature measured using an RTD.

to heat conversion. Applying adiabatic assumptions and a negligible thermo-elastic thermal contribution, the transient heat conduction equation is modified resulting in the following expression for the conversion of plastic work to heat (β_{int}) [29,44].

$$\beta_{int}(\varepsilon) = \frac{\rho c_p \Delta T}{\int dW_p} \quad (6)$$

where, ρ is the material density, c_p is the heat capacity of the material, ΔT is the global temperature rise during plastic deformation, and $\int dW_p$ is the total plastic work.

In dynamic experiments, such as those conducted with the TSHPB, the time required to achieve a force balance prevents the initial portion of the stress-strain curve from accurately representing material behavior. This is a known limitation of Hopkinson (or Kolsky) bar techniques. The inaccuracy of the early stages of deformation makes it challenging to isolate the onset of plastic strain. Therefore, in the presented work, the entire stress-strain curve is integrated to calculate the total work experienced by the specimen. The significant ductility exhibited by IN718, minimizes the effect of including elastic work in β_{int} calculations. The density (ρ) used in all calculations is 8190 kg/m^3 and the material heat capacity was considered to be a constant value of 435 J/kg°C [60] over the range of temperatures observed during experiments. While the density of LPBF IN718 is known to vary based on build parameters used (e.g.,[61]), the manufacturer recommended parameters used to produce the as-built condition as well as the extraction of specimens from the interior of the build volume result in a material that is approximated as fully dense.

3. Results and discussion

3.1. Microstructure characterization

A collection of BSE micrographs were captured to highlight the qualitative differences of the three material conditions examined (Fig. 4). The wrought condition, Fig. 4(a), has an equiaxed grain structure with the δ phase precipitated at grain boundaries. A similar magnification image of the as-built LPBF condition is shown in Fig. 4(b). During the rapid solidification intrinsic to LPBF, segregation regions develop, creating an intragranular cellular structure. Within the segregation regions the Laves phase is predominant, with some groups reporting the observation of γ' and carbide phases [62,63]. As has been observed previously, the cellular structure orientation can vary over a single grain [64]. Lastly, the recrystallized condition is shown in Fig. 4 (c). The recrystallized condition consists of large equiaxed grains. Compared to the as-built condition, it is apparent that the recrystallizing heat treatment has successfully dissolved the Laves phase. Carbide particles, indicated by arrow heads, have a melting temperature well above the recrystallization temperature of IN718. The carbide particles decorate grain boundaries and act as pinning sites for grain growth.

Quantitative descriptors of grain size and morphology for each microstructure, as well as crystallographic texture were determined from EBSD measurements. An inverse pole figure with grain orientation coloring is provided for the wrought, as-built, and recrystallized conditions in Fig. 5(a), (c) and (e), respectively. Corresponding pole figure triads for each condition are provided in Fig. 5(b), (d), and (f), respectively. Material grain sizes for the wrought and recrystallized condition (i.e., equiaxed conditions) were determined using the line intercept method in a single plane. The elongated grain morphology of the as-built condition required performing grain size measurements on planes normal to each principal processing direction. The wrought condition was determined to have an average grain size of 7.9 μm and a standard deviation of 4.1 μm. The average grain size of the as-built condition was found to be 22.1 μm with a standard deviation of 10.4 μm. The recrystallized condition had a grain size of 94.7 μm with a standard deviation of 41.2 μm, which is roughly an order of magnitude larger than the wrought condition.

The pole figure triads for each material condition exhibit unique textures. As would be expected due to its processing, the wrought material exhibits a texture resembling the rolling texture of an fcc material. The as-built condition has a $\langle 100 \rangle$ fiber texture aligned to the build direction caused by the $\langle 100 \rangle$ direction being the most favored solidification direction of fcc materials [65], and the thermal gradient which is aligned to the build direction in the LPBF process. The observed $\langle 100 \rangle$ texture is consistent with previously reported AM IN718 texture observations (e.g., [64,66]). The recrystallized condition texture is random as would be expected from a heat treatment that exceeds the recrystallization temperature of IN718.

3.2. Thermo-mechanical behavior

A total of 9 specimens were included in the study (3 replicates for each condition). With the exception of one recrystallized specimen, multiple loading increments were necessary to fail specimens, as shown in Fig. 6. Wrought IN718 exhibited the greatest strain to failure, followed by the as-built and recrystallized conditions, respectively. The material with the greatest tensile yield strength is the recrystallized condition, followed by the as-built and wrought conditions, respectively. During each loading increment, the specimen stress-strain behavior and corresponding temperature rise were recorded as is shown in Fig. 7.

For each loading increment, a single value estimate for the conversion of plastic work to heat (β_{avg}) is determined from the average value of β_{int} over the experiment duration. β_{avg} is determined by dividing the slope of the linear fit between the temperature rise and work density by the product of the material density (ρ) and heat capacity (c_p) (i.e., a rearrangement of Equation 6). As shown in Fig. 8, it was found that a linear relationship between the temperature rise and work density was present for the loading increments when necking did not occur. For the wrought material, necking takes place during the final loading increment. When necking occurs outside (or inside) of the IR detector interrogation region a non-representative specimen temperature rise will be recorded. The complete evolution of β_{int} can be calculated as a function

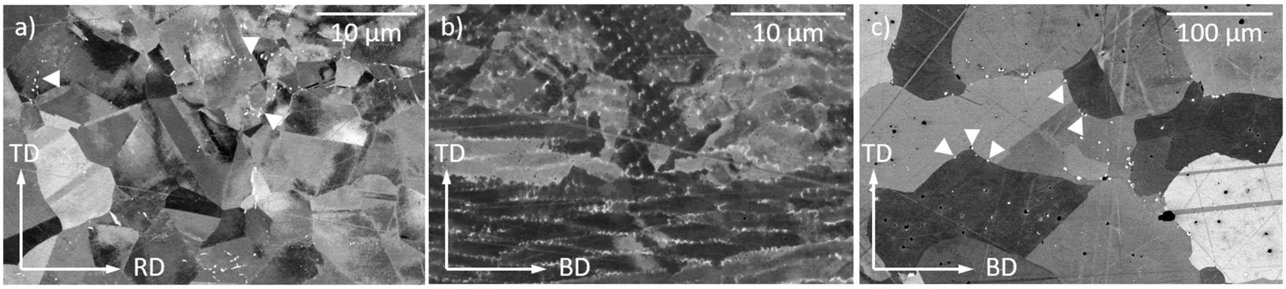

Fig. 4. BSE micrographs of the a) wrought, b) as-built and c) recrystallized condition illustrate the predominant phase distributions for each material condition. Arrow heads in a) indicate the grain boundary delta phases, and in c) indicate the grain boundary carbide phase.

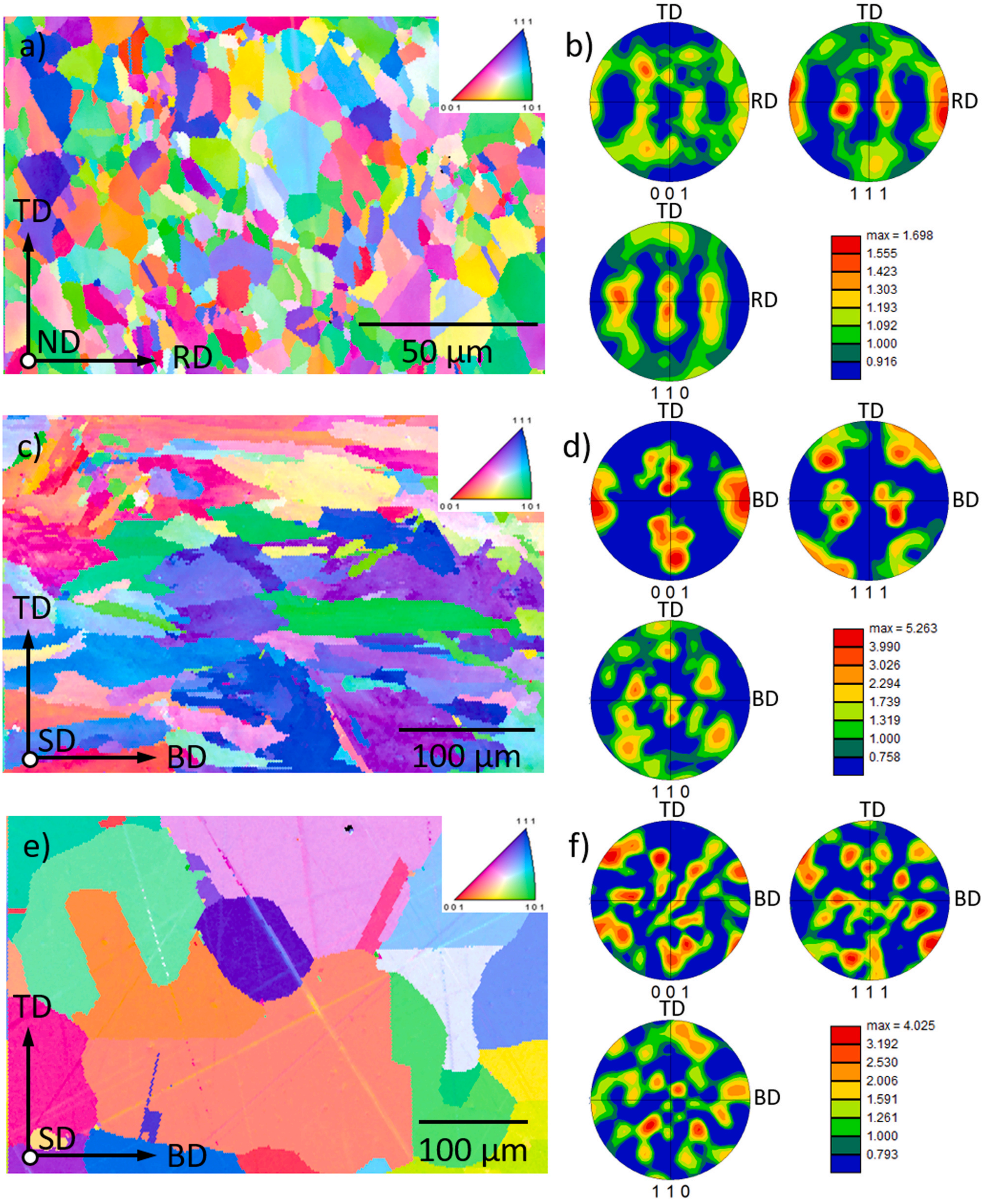

Fig. 5. Inverse pole figure with orientation coloring.

of strain, see Fig. 8(b). The dashed lines in Fig. 8 provide upper and lower error bounds of β_{int} assuming a ± 0. 2° C temperature variation. This ± 0. 2° is the accuracy limit of the RTD used during the IR detector calibration. The error range is exaggerated at low strain values due to the limited work density accumulated by the specimen.

Fig. 9, presents a summary of the single valued conversion of plastic work to heat efficiency (β_{avg}) for loading increments having a linear relationship between temperature rise and work density. The complete evolution of β_{int} for each specimen condition for all deformation increments is provided in Fig. 10. Regardless of the representation of the conversion of plastic work to heat, it can be seen that there is variability in the β_{avg} and β_{int} calculated for specimens of a given material condition as well as between each material condition.

A summary of the single valued β_{avg} values from each specimen and

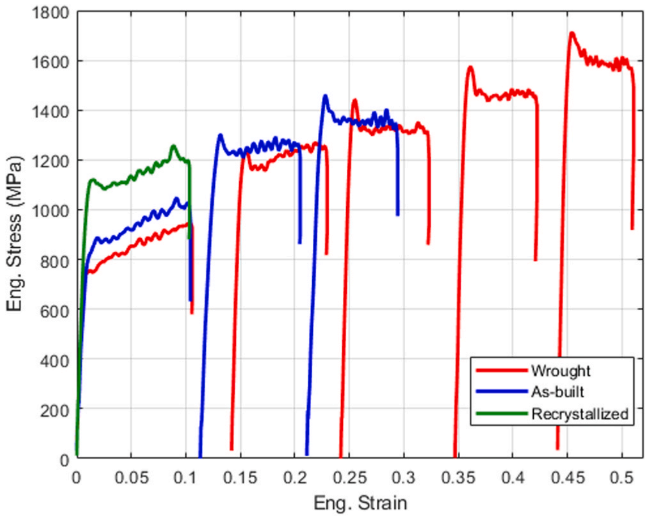

Fig. 6. Representative stress-strain curves for incrementally loaded wrought, LPBF as-built, and recrystallized IN718. The average strain rate of each loading increment shown is 460 s^{-1}, with a range of ± 60 s^{-1}.

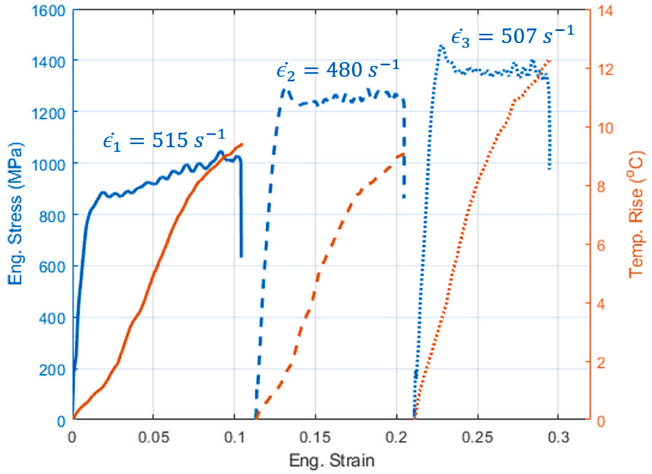

Fig. 7. Stress-strain behavior for an incrementally loaded as-built LPBF IN718 specimen and the temperature rise recorded for each loading increment. The strain rate for each loading increment is provided above its respective stress-strain curve.

the average and standard deviations for each specimen condition group are provided in Table 1. The wrought condition had the lowest single value plastic work to heat conversion ($\beta_{avg} = 0.166$), the as-built condition had an intermediate value ($\beta_{avg} = 0.262$), and the recrystallized condition had the greatest single value work to heat conversion ($\beta_{avg} = 0.482$). A one-way analysis of variance (ANOVA) was performed after grouping measurements from each specimen condition. A statistically significant difference ($p < 0.05$) was found between the mean β_{avg} measured for each specimen condition; $p < 0.02$ for wrought vs. as-built, $p < 0.01$ for wrought vs. recrystallized, $p < 0.01$ for as-built vs. recrystallized.

The source of the inter-specimen variability for a single material condition can be attributed to limitations associated the use of a single 100 μm by 100 μm element IR-detector to monitor the heterogeneous deformation process. The Newtonian optical system utilized has a magnification of one. Therefore as the material grain size increases, the IR detector transitions from sampling hundreds of grains deforming for the wrought condition, to tens of grains of as-built condition, to just a handful of grains of the recrystallized condition. The direct outcome of sampling less grains during deformation is an increase in the observed variability in β_{int} with increasing grain size. An additional source of variability in β_{int} as function of strain is due to the IR detector remaining fixed in space, while the specimen translates during deformation. Thus, the IR measurements represent a line scan measurement and do not represent the tracking of a single point on the specimen throughout the experiment duration.

The wrought condition had the lowest β_{int}, the recrystallized condition had the highest, and the as-built condition was between the wrought and recrystallized conditions. Despite exhibiting different plastic work to heat efficiencies, all material conditions accommodate plasticity through the same dislocation mechanism, massive planar slip [2]. The corollary to the conversion of plastic work to heat is the concept of stored energy, $f = 1 - \beta$. An overview of the concept of stored energy can be found in Ref. [28]. Adopting the concept of stored energy, the wrought condition had the greatest stored energy capability, followed by the as-built condition, and the recrystallized condition, respectively. The following favors using discussions of the conversion of plastic work to heat or using stored energy as is necessary to enable discussion and comparison to literature. Table 2 presents and overview of the dramatically different microstructures represented by the wrought, as-built and recrystallized material conditions.

3.3. *Coherency hardening*

The strength of IN718 is primarily attributed to the coherency hardening of the γ'' precipitates with the γ' precipitates playing a comparatively limited role. Two of the three material conditions investigated have dense γ' and γ'' precipitation networks. The wrought condition can be considered to be of an appropriately aged state containing an optimized distribution of γ' and γ'' phases due it having been prepared in accordance with AMS 5596 [53]. The recrystallized condition was characterized using high-resolution transmission electron microscopy, finding a uniform distribution of the γ' and γ'' throughout [67]. Both the wrought and recrystallized condition are aged in a stress-free state (i.e., no external force application) and therefore it is unlikely that the γ'' phase in either material condition has a global orientation preference. Thus, the dislocation interactions with the γ'' phase are presumed to be similar for the wrought and recrystallized conditions. The as-built condition is likely to be devoid of the γ' and γ'' phases. This claim is supported by previous investigations having rarely observed the γ' and γ'' phases in the as-built condition [51,68–70].

Comparing the defect storage capability of the three material conditions points to the presence (or absence) of the γ' and γ'' phase as not being the dominant microstructural feature in governing the difference in the materials plastic work to heat conversion efficiency (β). If coherency hardening was a dominant effect on β, one would expect the wrought condition and the recrystallized condition to show better agreement in their conversion of plastic work to heat. Fig. 9 shows the wrought and recrystallized state are the upper and lower bounds of the three conditions examined.

3.4. *Initial dislocation density*

IN718 in the as-built condition produced using LPBF is known to have a high initial dislocation density manifesting as dense dislocation cell networks. Recent characterization of the three-dimensional distribution of geometrically necessary dislocations (GNDs) found intra-granular sub-boundaries having GND densities in the range of 1×10^{13} to 8×10^{13} m^{-2} [71]. A transmission-electron-microscope-based investigation of as-built LPBF IN718 has also found significant lattice dislocation densities on the order of $1.6 \pm 0.8 \times 10^{14}$ m^{-2} at intragranular sub-boundaries [51]. These dislocation-rich sub-boundaries are known to extend throughout grains. The elevated initial dislocation densities observed in the as-built condition, will reduce the material's overall defect storage capability and hinder the motion of glissile dislocations during

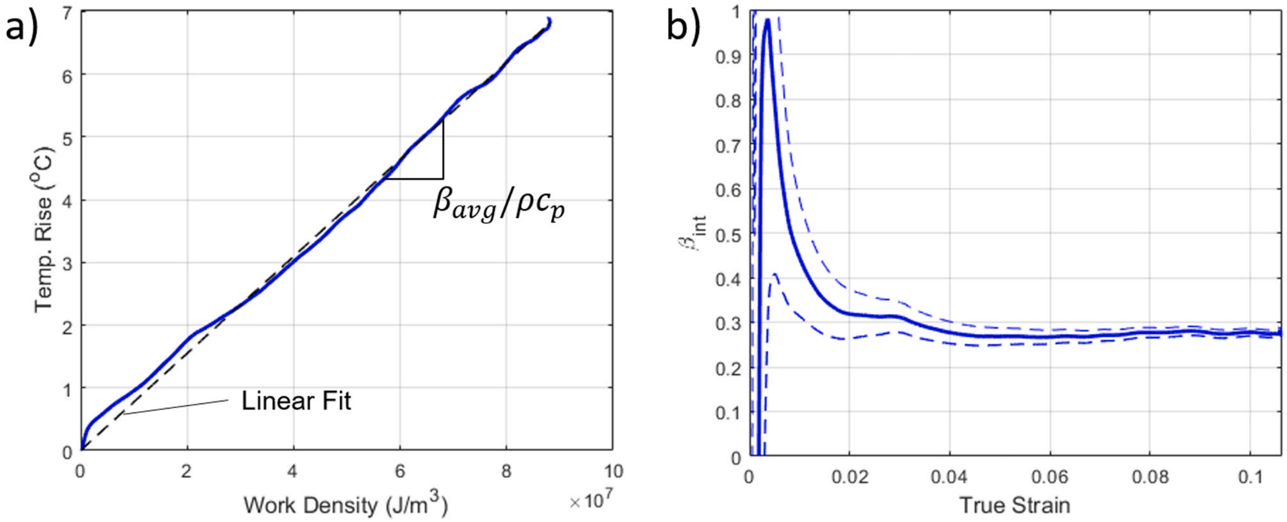

Fig. 8. Conversion of plastic work to heat when a) assuming a single valued efficiency over the loading increment, and b) calculating the evolution of beta during plastic strain accumulation.

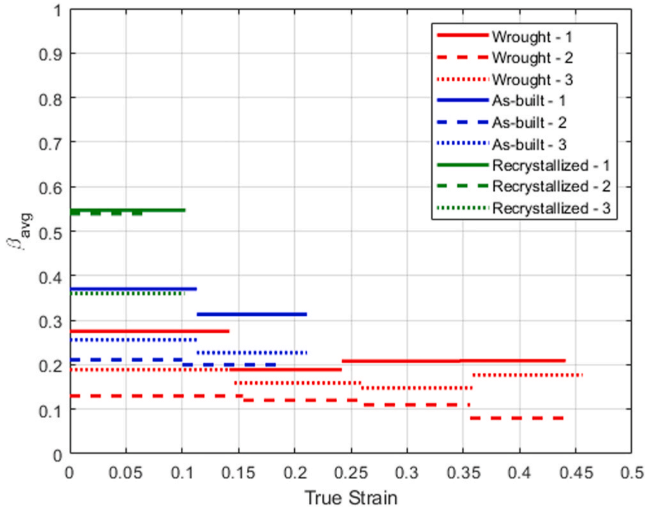

Fig. 9. Conversion of plastic work to heat when assuming a single valued efficiency over the loading increment. All experiments were conducted at a strain rate of 460 ± 60 s^{-1}.

deformation. A reduction in defect storage capability will result in an appreciable increase in a material's plastic work to heat conversion compared to a material system, such as the annealed wrought material, whose low initial dislocation density has a greater defect storage capacity.

Recrystallized and well annealed materials are typically approximated as having dislocation densities on the order of 10^{11} m^{-2} [72]. Comparing the wrought condition (low dislocation density) to the

Table 1
Summary of β_{avg}.

Specimen No.	Specimen Condition		
	Wrought	As-Built	Recrystallized
1	0.220	0.341	0.547
2	0.110	0.205	0.539
3	0.168	0.241	0.360
Average	0.166	0.262	0.482
Std. Dev.	0.053	0.066	0.105

Table 2
Summary of qualitative and quantitative microstructural features of each investigated material condition.

Material condition	Primary phases (γ' and γ'')	Dislocation cells	Secondary δ phase	Grain size (μm)
Wrought	Yes	No	No	7.9 ± 4.1
As-built	No[51]	Yes[51]	Limited	22.1 ± 10.4
Recrystallized	Yes[67]	No[67]	Yes - Grain boundaries	94.7 ± 41.2

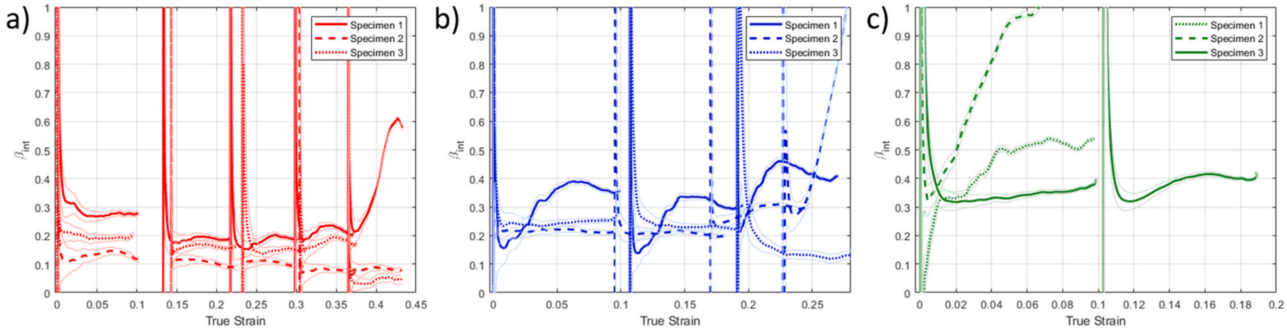

Fig. 10. Conversion of plastic work to heat as a function of strain for the a) wrought, b) as-built LPBF, and c) recrystallized material condition. Experiments were conducted at an average strain rate of 460 with the complete range of strain-rates across all experiments being ± 60 s^{-1}.

as-built condition (high dislocation density), it takes a roughly two orders of magnitude increase in the initial dislocation density to increase the conversion of plastic work to heat by $\approx 10\%$. A two orders of magnitude increase of initial dislocation density is substantial and is comparable to the total number of dislocations accumulated by a well-annealed material as it becomes heavily deformed. Therefore, it is proposed for the IN718 material system, that dislocation density contributes less to the conversion of plastic work to heat than other microstructural features. This observation is supported by investigations of slip dominated fcc materials such Al 2024, which presented a near-constant plastic work to heat conversion after the accumulation of a few percent strain up to failure [35].

3.5. Secondary phases

In addition to the γ' and γ'' phases, the δ phase is known to influence material properties. Among the three material preparation conditions, the δ phase is predominantly observed at grain boundaries in the recrystallized condition [67]. As the δ phase presence increases, the ductility of IN718 decreases [73–75]. When dislocations pile-up at the δ phase- matrix interface, cleavage cracks separate the δ phase. Temperature rises associated with the propagating cracks can be significant compared to temperature rises associated with plastic deformation. For example, Guduru et al. reported temperature rises in front of cracks propagating in C300 steel to be on the order of 200 °C [76], a value significantly above the ≈ 25 °C temperature rise reported for the same material system deforming plasticity by Rittel et al. [34]. While temperatures associated with microcracking are significantly higher than those associated with uniform deformation, the length scale of microcracking (i.e. a few microns) and the adiabatic nature of deformation would limit its influence on measurements due to the limited number of grains sampled during deformation. Thus, it is proposed that even though the delta phase significantly decreases the ductility of IN718 it has limited impact on the material’s conversion of plastic work to heat.

3.6. Grain size

The Taylor-Quinney coefficient of the three IN718 material conditions investigated increases with grain size. Thus, the stored energy is higher for smaller grain sizes and lower for larger grain sizes. This observation is in agreement with recent simulation efforts (e.g., [47]) and previous experimental (e.g., [77,78]). Kositski and Mordehai [47] concluded that grain boundaries play a dual role as both a source for energy storage and of energy release. Therefore the density of grain boundaries will directly impact the work to heat conversion. The experimental work by Oliferuk et al. [37,79] investigated the energy storage efficiency of austenitic stainless steel deformed in tension at grain sizes of 8 μm and 80 μm, which are similar to the wrought and recrystallized conditions investigated in the current study. Oliferuk et al. found that energy storage was sensitive to grain size predominantly during the initial stages of deformation ($\epsilon < 0.05$) while “easy” primary slip processes are operative. Once exhausted and higher energy dislocation configurations become active (e.g., pile-ups), there was a reduction in the difference between the energy storage efficiency of the two grain sizes. A variation in energy storage (or Taylor-Quinney coefficient) as a function of strain was not conclusively observed in the current work. Therefore it is proposed that there is not a transition between primary and secondary deformation mechanisms that would impact the energy storage capability of IN718 in any of the conditions examined.

Numerous investigators have highlighted the importance of grain boundaries and the interaction of dislocations with them when discussing energy storage and the conversion of plastic work to heat. For example, Oliferuk et al proposed that the storage efficiency is no longer grain size dependent once secondary slip systems are activated near grain boundaries [79], and that an additional energy storage source is the elastic energy contained in the near grain boundary stress fields [37]. Future work using relevant techniques including transmission electron microscopy to capture dislocation arrangements and high resolution electron backscatter diffraction to assess elastic strains near grain boundaries is planned to attempt to further refine understanding of the role that dislocations and sub-grain stress fields play on energy storage and the conversion of plastic work to heat in the IN718 material system.

4. Conclusions

The current study presents a systematic investigation of the plastic work to heat conversion efficiency of the important aerospace alloy IN718. Three preparation conditions were examined, namely the wrought condition, LPBF as-built, and LPBF recrystallized condition. Measurements of the plastic work to heat conversion efficiency (i.e., Taylor-Quinney coefficient) are considerably smaller than the commonly assumed value of $\beta = 0.9$. From the experiments performed, it is observed that initial dislocation density has a limited contribution to β in a deformation-slip dominated material. Coherency hardening conferred by the primary strengthening phases γ' and γ'' also appears to have a limited effect on β based on the coherency hardened wrought condition and recrystallized condition having significantly different plastic work to heat conversion efficiencies. The presence of the δ phase at the grain boundary is proposed to be a strong influencing factor on overall material ductility, but the microcracking and cleavage of the delta phase that precedes failure is at such a small length scale that it is believed to have negligible influence in reported measurements. Among the discussed microstructural features, grain size and therefore grain boundary density appears to be the dominant contributor to the conversion of plastic work to heat in IN718 for the material conditions examined. Taken together the current work suggests the need to carefully assess the Taylor-Quinney coefficient for AM materials as their plastic work to heat conversion efficiencies can be substantially altered by post-build heat treatments that manipulate grain size. Furthermore, there are ripe opportunities for continued experimental and simulation efforts to refine understanding of the role that dislocation interactions and grain boundaries play on the work to heat conversion in metals.

CRediT authorship contribution statement

J. Varga: Writing – original draft, Investigation. **O.T. Kingstedt:** Conceptualization, Funding acquisition, Supervision, Writing – review & editing.

Declaration of Competing Interest

The authors declare that they have no known competing financial interests or personal relationships that could have appeared to influence the work reported in this paper.

Acknowledgments

The research described herein was supported by the Department of Defense Office of Economic Adjustment under award no. ST1605-19-03 and the National Science Foundation CAREER award no. 1847653. This work made use of University of Utah shared facilities of the Micron Technology Foundation Inc. Microscopy Suite sponsored by the College of Engineering, Health Sciences Center, Office of the Vice President for Research, and the Utah Science Technology and Research (USTAR) initiative of the State of Utah. This work also made use of University of Utah USTAR shared facilities supported, in part, by the MRSEC Program of the NSF under Award No. DMR-1121252.

References

[1] R. Cozar, A. Pineau, Morphology of $\gamma'$and γ'' precipitates and thermal stability of inconel 718 type alloys, Metall. Trans. 4 (1973) 47–59.

[2] D. Paulonis, J. Oblak, D. Duvall, Precipitation in nickel-base alloy 718, Trans. Am. Soc. Met. 62 (1969) 611–622.

[3] M. Sundararaman, P. Mukhopadhyay, S. Banerjee, Some aspects of the precipitation of metastable intermetallic phases in inconel 718, Metall. Trans. A 23 (1992) 2015–2028.

[4] F.C. Campbell, Elements of Metallurgy and Engineering Alloys, ASM International, 2008.

[5] D. Lv, D. McAllister, M. Mills, Y. Wang, Deformation mechanisms of d022 ordered intermetallic phase in superalloys, Acta Mater. 118 (2016) 350–361.

[6] D. McAllister, D. Lv, B. Peterson, H. Deutchman, Y. Wang, M. Mills, Lower temperature deformation mechanisms in a γ''-strengthened ni-base superalloy, Scr. Mater. 115 (2016) 108–112.

[7] R.M. Nunes, D. Pereira, T. Clarke, T.K. Hirsch, Delta phase characterization in inconel 718 alloys through x-ray diffraction, ISIJ Int. 55 (2015) 2450–2454.

[8] S. Azadian, L.-Y. Wei, R. Warren, Delta phase precipitation in inconel 718, Mater. Charact. 53 (2004) 7–16.

[9] E. Hosseini, V. Popovich, A review of mechanical properties of additively manufactured inconel 718, Addit. Manuf. 30 (2019), 100877.

[10] D. Deng, Additively Manufactured Inconel 718: Microstructures and Mechanical Properties, volume 1798, Linköping University Electronic Press, 2018.

[11] D. Brown, C. Li, Z. Liu, X. Fang, Y. Guo, Surface integrity of inconel 718 by hybrid selective laser melting and milling, Virtual Phys. Prototyp. 13 (2018) 26–31.

[12] M., Ichimura, Y., Urushisaki, K., Amaya, S., Chappell, M., Honnami, M., Mochizuki, U., Chung, Medical implant manufacture using the hybrid metal laser sintering with machining process, in: Proceedings of the 15th International Conference on Precision Engineering (ICPE), Kanazawa, Japan, July, pp. 22–25.

[13] M. Rahman, W. Seah, T. Teo, The machinability of inconel 718, J. Mater. Process. Technol. 63 (1997) 199–204.

[14] D. Thakur, B. Ramamoorthy, L. Vijayaraghavan, A study on the parameters in high-speed turning of superalloy inconel 718, Mater. Manuf. Process. 24 (2009) 497–503.

[15] M. Tang, P.C. Pistorius, J.L. Beuth, Prediction of lack-of-fusion porosity for powder bed fusion, Addit. Manuf. 14 (2017) 39–48.

[16] G. Vastola, Q. Pei, Y.-W. Zhang, Predictive model for porosity in powder-bed fusion additive manufacturing at high beam energy regime, Addit. Manuf. 22 (2018) 817–822.

[17] F. Imani, A. Gaikwad, M. Montazeri, P. Rao, H. Yang, E. Reutzel, Process mapping and in-process monitoring of porosity in laser powder bed fusion using layerwise optical imaging, J. Manuf. Sci. Eng. 140 (2018).

[18] H.D. Carlton, A. Haboub, G.F. Gallegos, D.Y. Parkinson, A.A. MacDowell, Damage evolution and failure mechanisms in additively manufactured stainless steel, Mater. Sci. Eng.: A 651 (2016) 406–414.

[19] H. Gong, K. Rafi, H. Gu, G.J. Ram, T. Starr, B. Stucker, Influence of defects on mechanical properties of ti–6al–4 v components produced by selective laser melting and electron beam melting, Mater. Des. 86 (2015) 545–554.

[20] L. Sheridan, O.E. Scott-Emuakpor, T. George, J.E. Gockel, Relating porosity to fatigue failure in additively manufactured alloy 718, Mater. Sci. Eng.: A 727 (2018) 170–176.

[21] N. Kouraytem, X. Li, R. Cunningham, C. Zhao, N. Parab, T. Sun, A.D. Rollett, A. D. Spear, W. Tan, Effect of laser-matter interaction on molten pool flow and keyhole dynamics, Phys. Rev. Appl. 11 (2019), 064054.

[22] W.E. King, H.D. Barth, V.M. Castillo, G.F. Gallegos, J.W. Gibbs, D.E. Hahn, C. Kamath, A.M. Rubenchik, Observation of keyhole-mode laser melting in laser powder-bed fusion additive manufacturing, J. Mater. Process. Technol. 214 (2014) 2915–2925.

[23] D.S. Watring, J.T. Benzing, N. Hrabe, A.D. Spear, Effects of laser-energy density and build orientation on the structure–property relationships in as-built inconel 718 manufactured by laser powder bed fusion, Addit. Manuf. 36 (2020), 101425.

[24] B.B. Babamiri, J. Indeck, G. Demeneghi, J. Cuadra, K. Hazeli, Quantification of porosity and microstructure and their effect on quasi-static and dynamic behavior of additively manufactured inconel 718, Addit. Manuf. 34 (2020), 101380.

[25] P. Kumar, J. Farah, J. Akram, C. Teng, J. Ginn, M. Misra, Influence of laser processing parameters on porosity in inconel 718 during additive manufacturing, Int. J. Adv. Manuf. Technol. 103 (2019) 1497–1507.

[26] W.S. Farren, G.I. Taylor, The heat developed during plastic extension of metals, Proc. R. Soc. Lond. Ser. A 107 (1925) 422–451.

[27] G.I. Taylor, H. Quinney, The latent energy remaining in a metal after cold working, Proc. R. Soc. Lond. Ser. A 143 (1934) 307–326.

[28] M.B. Bever, D.L. Holt, A.L. Titchener, The stored energy of cold work, Prog. Mater. Sci. 17 (1973) 5–177.

[29] D. Rittel, On the conversion of plastic work to heat during high strain rate deformation of glassy polymers, Mech. Mater. 31 (1999) 131–139.

[30] J. Hodowany, G. Ravichandran, A. Rosakis, P. Rosakis, Partition of plastic work into heat and stored energy in metals, Exp. Mech. 40 (2000) 113–123.

[31] D. Rittel, A. Kidane, M. Alkhader, A. Venkert, P. Landau, G. Ravichandran, On the dynamically stored energy of cold work in pure single crystal and polycrystalline copper, Acta Mater. 60 (2012) 3719–3728.

[32] D. Rittel, Z.G. Wang, M. Merzer, Adiabatic shear failure and dynamic stored energy of cold work, Phys. Rev. Lett. 96 (2006), 075502.

[33] R. Clifton, J. Duffy, K. Hartley, T. Shawki, On critical conditions for shear band formation at high strain rates, Scr. Metall. 18 (1984) 443–448.

[34] D. Rittel, L. Zhang, S. Osovski, The dependence of the taylor–quinney coefficient on the dynamic loading mode, J. Mech. Phys. Solids 107 (2017) 96–114.

[35] J. Mason, A. Rosakis, G. Ravichandran, On the strain and strain rate dependence of the fraction of plastic work converted to heat: an experimental study using high speed infrared detectors and the kolsky bar, Mech. Mater. 17 (1994) 135–145.

[36] D. Ghosh, O.T. Kingstedt, G. Ravichandran, Plastic work to heat conversion during high-strain rate deformation of mg and mg alloy, Metall. Mater. Trans. A 48 (2017) 14–19.

[37] W. Oliferuk, A. Korbel, M.W. Grabski, Mode of deformation and the rate of energy storage during uniaxial tensile deformation of austenitic steel, Mater. Sci. Eng.: A 220 (1996) 123–128.

[38] R. Williams, The stored energy in deformed copper: the effect of grain size and silver content, Acta Metall. 9 (1961) 949–957.

[39] M. Loretto, A. White, The influence of grain size on the energy stored in deformed copper, Acta Metall. 9 (1961) 512–513.

[40] D. Rittel, M. Silva, B. Poon, G. Ravichandran, Thermomechanical behavior of single crystalline tantalum in the static and dynamic regime, Mech. Mater. 41 (2009) 1323–1329.

[41] O.T. Kingstedt, J.T. Lloyd, On the conversion of plastic work to heat in mg alloy az31b for dislocation slip and twinning deformation, Mech. Mater. 134 (2019) 176–184.

[42] A.T. Zehnder, A model for the heating due to plastic work, Mech. Res. Commun. 18 (1991) 23–28.

[43] N. Aravas, K. Kim, F. Leckie, On the calculations of the stored energy of cold work, J. Eng. Mater. Technol. 112 (1990) 465–470.

[44] R. Kapoor, S. Nemat-Nasser, Determination of temperature rise during high strain rate deformation, Mech. Mater. 27 (1998) 1–12.

[45] P. Rosakis, A. Rosakis, G. Ravichandran, J. Hodowany, A thermodynamic internal variable model for the partition of plastic work into heat and stored energy in metals, J. Mech. Phys. Solids 48 (2000) 581–607.

[46] A. Benzerga, Y. Bréchet, A. Needleman, E. Van der Giessen, The stored energy of cold work: Predictions from discrete dislocation plasticity, Acta Mater. 53 (2005) 4765–4779.

[47] R. Kositski, D. Mordehai, Employing molecular dynamics to shed light on the microstructural origins of the taylor-quinney coefficient, Acta Mater. 205 (2021), 116511.

[48] C.K. Lieou, C.A. Bronkhorst, Thermomechanical conversion in metals: dislocation plasticity model evaluation of the taylor-quinney coefficient, Acta Mater. 202 (2021) 170–180.

[49] D. Macdougall, J. Harding, The measurement of specimen surface temperature in high-speed tension and torsion tests, Int. J. Impact Eng. 21 (1998) 473–488.

[50] X.R.S. YangBaochang, An infrared transient temperature measuring apparatus and its application to the tensile impact testing, J. Exp. Mech. 2 (1990).

[51] T.G. Gallmeyer, S. Moorthy, B.B. Kappes, M.J. Mills, B. Amin-Ahmadi, A. P. Stebner, Knowledge of process-structure-property relationships to engineer better heat treatments for laser powder bed fusion additive manufactured inconel 718, Addit. Manuf. 31 (2020), 100977.

[52] ASTM B670–18, Standard Specification for Precipitation-Hardening Nickel Alloy (UNS N07718) Plate, Sheet, and Strip for High-Temperature Service, Standard, ASTM International, 2018.

[53] AMS5596M, Nickel Alloy, Corrosion and Heat-Resistant, Sheet, Strip, Foil and Plate 52.5Ni - 19Cr - 3.0Mo - 5.1Cb (Nb) - 0.90Ti - 0.50Al - 18Fe Consumable Electrode Remelted or Vacuum Induction Melted 1775 ˚F (968 ˚C) Solution Heat Treated, Standard, SAE International, 2017.

[54] S. Moorthy, Modeling and Characterization of Mechanical Properties in Laser Powder Bed Fusion Additive Manufactured Inconel 718, Colorado School of Mines, 2018.

[55] C. Kantzos, J. Pauza, R. Cunningham, S.P. Narra, J. Beuth, A. Rollett, An investigation of process parameter modifications on additively manufactured inconel 718 parts, J. Mater. Eng. Perform. 28 (2019) 620–626.

[56] A. Zehnder, E. Babinsky, T. Palmer, Hybrid method for determining the fraction of plastic work converted to heat, Exp. Mech. 38 (1998) 295–302.

[57] B.A. Gama, S.L. Lopatnikov, J.W. Gillespie Jr, Hopkinson bar experimental technique: a critical review, Appl. Mech. Rev. 57 (2004) 223–250.

[58] W.W. Chen, B. Song, Split Hopkinson (Kolsky) Bar: Design, Testing and Applications, Springer Science & Business Media, 2010.

[59] J., Hodowany, On the Conversion of Plastic Work into Heat, Ph.D. thesis, California Institute of Technology, 1997.

[60] J.J. DeMange, V. Prakash, J.M. Pereira, Effects of material microstructure on blunt projectile penetration of a nickel-based super alloy, Int. J. Impact Eng. 36 (2009) 1027–1043.

[61] G.E. Bean, D.B. Witkin, T.D. McLouth, D.N. Patel, R.J. Zaldivar, Effect of laser focus shift on surface quality and density of inconel 718 parts produced via selective laser melting, Addit. Manuf. 22 (2018) 207–215.

[62] L.L. Parimi, G. Ravi, D. Clark, M.M. Attallah, Microstructural and texture development in direct laser fabricated in718, Mater. Charact. 89 (2014) 102–111.

[63] E. Chlebus, K. Gruber, B. Kuźnicka, J. Kurzac, T. Kurzynowski, Effect of heat treatment on the microstructure and mechanical properties of inconel 718 processed by selective laser melting, Mater. Sci. Eng.: A 639 (2015) 647–655.

[64] D. Deng, R.L. Peng, H. Brodin, J. Moverare, Microstructure and mechanical properties of inconel 718 produced by selective laser melting: sample orientation dependence and effects of post heat treatments, Mater. Sci. Eng.: A 713 (2018) 294–306.

[65] R.C. Reed, The Superalloys: Fundamentals and Applications, Cambridge University Press, 2008.

[66] L.N. Carter, C. Martin, P.J. Withers, M.M. Attallah, The influence of the laser scan strategy on grain structure and cracking behaviour in slm powder-bed fabricated nickel superalloy, J. Alloy. Compd. 615 (2014) 338–347.

[67] N. Kouraytem, J. Varga, B. Amin-Ahmadi, H. Mirmohammad, R.A. Chanut, A. D. Spear, O.T. Kingstedt, A recrystallization heat-treatment to reduce deformation anisotropy of additively manufactured Inconel 718, Mater. Des. 198 (2021), 109228.

[68] D. Zhang, W. Niu, X. Cao, Z. Liu, Effect of standard heat treatment on the microstructure and mechanical properties of selective laser melting manufactured inconel 718 superalloy, Mater. Sci. Eng.: A 644 (2015) 32–40.

[69] W.M. Tucho, P. Cuvillier, A. Sjolyst-Kverneland, V. Hansen, Microstructure and hardness studies of inconel 718 manufactured by selective laser melting before and after solution heat treatment, Mater. Sci. Eng.: A 689 (2017) 220–232.

[70] X. Li, J. Shi, C. Wang, G. Cao, A. Russell, Z. Zhou, C. Li, G. Chen, Effect of heat treatment on microstructure evolution of inconel 718 alloy fabricated by selective laser melting, J. Alloy. Compd. 764 (2018) 639–649.

[71] W.A. Witzen, A.T. Polonsky, T.M. Pollock, I.J. Beyerlein, Three-dimensional maps of geometrically necessary dislocation densities in additively manufactured ni-based superalloy in718, Int. J. Plast. (2020), 102709.

[72] W.D. Callister Jr, D.G. Rethwisch, Fundamentals of Materials Science and Engineering: An Integrated Approach, John Wiley & Sons, 2020.

[73] X.-P. Wei, W.-J. Zheng, Z.-G. Song, T. Lei, Q.-L. Yong, Q.-C. Xie, Strain-induced precipitation behavior of δ phase in inconel 718 alloy, J. Iron Steel Res. Int. 21 (2014) 375–381.

[74] J.F., Radavich, G., Korth, High temperature degradation of alloy 718, in: Proceedings of Seventh International Symposium on Superalloys, Seven Springs, MD, pp. 497–506.

[75] Y.-L. Kuo, S. Horikawa, K. Kakehi, The effect of interdendritic δ phase on the mechanical properties of alloy 718 built up by additive manufacturing, Mater. Des. 116 (2017) 411–418.

[76] P. Guduru, A. Zehnder, A. Rosakis, G. Ravichandran, Dynamic full field measurements of crack tip temperatures, Eng. Fract. Mech. 68 (2001) 1535–1556.

[77] L. Clarebrough, M. Hargreaves, M. Loretto, The influence of grain size on the stored energy and mechanical properties of copper, Acta Metall. 6 (1958) 725–735.

[78] R. Williams, The stored energy of copper deformed at 24c, Acta Metall. 13 (1965) 163–168.

[79] W. Oliferuk, W. Swiatnicki, M.W. Grabski, Effect of the grain size on the rate of energy storage during the tensile deformation of an austenitic steel, Mater. Sci. Eng.: A 197 (1995) 49–58.